Prediction of the structures of free and oxide-supported nanoparticles by means of atomistic approaches: The benchmark case of nickel clusters

ARTICLE *in* PHYSICAL CHEMISTRY CHEMICAL PHYSICS · AUGUST 2010

Impact Factor: 4.49 · DOI: 10.1039/c003949g · Source: PubMed

6 AUTHORS, INCLUDING:

Giulia Rossi
Università degli Studi di Genova
55 PUBLICATIONS **1,630** CITATIONS
SEE PROFILE

Riccardo Ferrando
Università degli Studi di Genova
234 PUBLICATIONS **8,376** CITATIONS
SEE PROFILE

Giovanni Barcaro
Italian National Research Council
106 PUBLICATIONS **1,598** CITATIONS
SEE PROFILE

Alessandro Fortunelli
Italian National Research Council
210 PUBLICATIONS **3,986** CITATIONS
SEE PROFILE

This paper is published as part of a *PCCP* themed issue on solid state and cluster structure prediction

Guest Editors: Richard Catlow and Scott M. Woodley

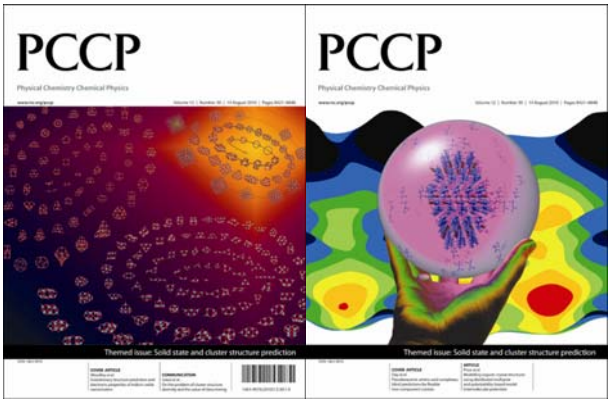

Editorial

Solid state and cluster prediction
Scott M. Woodley and Richard Catlow, *Phys. Chem. Chem. Phys.*, 2010
DOI: 10.1039/c0cp90058c

Communication

On the problem of cluster structure diversity and the value of data mining
Alexey A. Sokol, C. Richard A. Catlow, Martina Miskufova, Stephen A. Shevlin, Abdullah A. Al-Sunaidi, Aron Walsh and Scott M. Woodley, *Phys. Chem. Chem. Phys.*, 2010
DOI: 10.1039/c0cp00068j

Papers

Evolutionary structure prediction and electronic properties of indium oxide nanoclusters
Aron Walsh and Scott M. Woodley, *Phys. Chem. Chem. Phys.*, 2010
DOI: 10.1039/c0cp00056f

Exploration of multiple energy landscapes for zirconia nanoclusters
Scott M. Woodley, Said Hamad and C. Richard A. Catlow, *Phys. Chem. Chem. Phys.*, 2010
DOI: 10.1039/c0cp00057d

Pseudoracemic amino acid complexes: blind predictions for flexible two-component crystals
Carl Henrik Görbitz, Bjørn Dalhus and Graeme M. Day, *Phys. Chem. Chem. Phys.*, 2010
DOI: 10.1039/c004055j

Modelling organic crystal structures using distributed multipole and polarizability-based model intermolecular potentials
Sarah L. Price, Maurice Leslie, Gareth W. A. Welch, Matthew Habgood, Louise S. Price, Panagiotis G. Karamertzanis and Graeme M. Day, *Phys. Chem. Chem. Phys.*, 2010
DOI: 10.1039/c004164e

Ab initio prediction of low-temperature phase diagrams in the Al–Ga–In–As system, MAs–M´As (M, M´= Al, Ga or In) and AlAs–GaAs–InAs, *via* the global study of energy landscapes
Ilya V. Pentin, J. Christian Schön and Martin Jansen, *Phys. Chem. Chem. Phys.*, 2010
DOI: 10.1039/c004040c

Importance of London dispersion effects for the packing of molecular crystals: a case study for intramolecular stacking in a bis-thiophene derivative
Jonas Moellmann and Stefan Grimme, *Phys. Chem. Chem. Phys.*, 2010
DOI: 10.1039/c003432k

An extensive theoretical survey of low-density allotropy in silicon
Martijn A. Zwijnenburg, Kim E. Jelfs and Stefan T. Bromley, *Phys. Chem. Chem. Phys.*, 2010
DOI: 10.1039/c004375c

Predicting transition pressures for obtaining nanoporous semiconductor polymorphs: oxides and chalcogenides of Zn, Cd and Mg
Winyoo Sangthong, Jumras Limtrakul, Francesc Illas and Stefan T. Bromley, *Phys. Chem. Chem. Phys.*, 2010
DOI: 10.1039/c0cp00002g

Databases of virtual inorganic crystal structures and their applications
Armel Le Bail, *Phys. Chem. Chem. Phys.*, 2010
DOI: 10.1039/c003907c

Flexibility of ideal zeolite frameworks
V. Kapko, C. Dawson, M. M. J. Treacy and M. F. Thorpe, *Phys. Chem. Chem. Phys.*, 2010
DOI: 10.1039/c003977b

Constant pressure molecular dynamics simulations for ellipsoidal, cylindrical and cuboidal nano-objects based on inertia tensor information
Clive Bealing, Giorgia Fugallo, Roman Martoňák and Carla Molteni, *Phys. Chem. Chem. Phys.*, 2010
DOI: 10.1039/c004053c

Prediction of the structures of free and oxide-supported nanoparticles by means of atomistic approaches: the benchmark case of nickel clusters

Giulia Rossi,[a] Luca Anghinolfi,[b] Riccardo Ferrando,*[b] Florin Nita,[c] Giovanni Barcaro[d] and Alessandro Fortunelli*[d]

Received 5th March 2010, Accepted 8th June 2010
First published as an Advance Article on the web 28th June 2010
DOI: 10.1039/c003949g

The structures of Ni/MgO nanoparticles are studied by means of global optimization searches. The results from four different model potentials, sharing the same functional forms but different parametrizations, are reported and compared. Two parametrizations over four give qualitatively correct results, and one of them is also quantitatively satisfactory. The other models fail to explain some qualitative features observed in the experiments, such as the formation of hcp nanodots at small sizes or the transition to fcc structures at large sizes. The important features that an atomistic potential must present for the correct prediction of Ni cluster structures are discussed and generalized.

1. Introduction

Metal nanoparticles on oxide surfaces have been intensely studied in recent years because they are of great interest for applications in magnetism and catalysis.[1,2]

Depending on the oxide substrate and the metal, a rich variety of structures has been found. On the (001) surface of magnesium oxide, which is one of the most widely employed supports for model catalysts, by means of experiments[1,3–9] and calculations[10–22] several different structural motifs have been found. These motifs often resemble those found in gas-phase clusters, such as fcc truncated octahedra, or decahedral and icosahedral fragments. However, morphologies can also be specifically induced by the substrate, as in the case of hcp nickel nanoparticles or empty pyramidal gold cages on MgO(001).[4,17,21] For PtCo nanoparticles, the square-symmetry MgO(001) substrate enhances the stability of six-fold symmetry structures belonging to the polyicosahedral motif.[22] For these reasons, predicting the structures[23] of metal nanoparticles on MgO(001) is a very difficult task.

The Ni/MgO(001) system is of special interest from this point of view, because of its specific substrate-induced morphologies. This system was studied in ref. 17 by an approach combining different computational techniques: (a) global optimization searches within an atom–atom potential model to search for the low-energy structural motifs in the size range up to 500 atoms; (b) density-functional (DF) local relaxations for selected structures at small sizes, up to 50 atoms; (c) comparison of fcc and hcp structural motifs at geometric magic sizes, again within the atom–atom potential model, for sizes up to several thousand atoms. The results of the calculations were in very good agreement with the experimental findings of ref. 4, showing that hcp structures are the most energetically favourable in the diameter range 1–4.5 nm. These hcp structures are due to the rather strong interaction between Ni and MgO and to the lattice mismatch between the two systems. In fact, the nearest-neighbour distance in bulk Ni is 2.49 Å, whereas the distance between first-neighbour oxygen adsorption sites in MgO is of 2.98 Å. This large lattice mismatch strongly disfavours the simple cube-on-cube epitaxy of nanoparticles. This epitaxy is expected to be recovered when approaching the bulk limit (even though dislocations are expected too).

In this paper we focus on the aspects of the computational methodology that are crucial for predicting the correct morphology of supported nickel nanoparticles. To this purpose, we analyze the fitting procedure of the parameters of the atom–atom potential in order to single out what are the features that the potential must incorporate for a good quantitative description of nanoparticle morphologies. We consider four different parametrizations of the same functional form of the potential and demonstrate that they can predict quite different nanoparticle morphologies. This allows us to select the parametrization which is in better agreement with the experiments and to rationalize the reasons for its success, which will turn out to be of a rather general nature. Finally, for this parametrization we will compare the structures of free and oxide-supported aggregates, in order to explicitly show that the latter are specifically induced by the interaction with the substrate.

The paper is structured as follows. Section 2 contains the description of the interaction model and of the fitting procedure of the Ni–Ni potential. Two different parameter sets are derived and compared to other sets already available in the literature. Section 3 briefly describes the methodology employed to search for the low-energy motifs. Section 4

[a] *Dipartimento di Fisica, Università di Genova, Via Dodecaneso 33, 16146, Genova, Italy; Department of Applied Physics, Aalto University, P.O.Box 1100, FI-00076, Finland*
[b] *Dipartimento di Fisica, Università di Genova, Via Dodecaneso 33, 16146, Genova, Italy, Dipartimento di Fisica, Università di Genova, Via Dodecaneso 33, 16146, Genova, Italy. E-mail: ferrando@fisica.unige.it*
[c] *Institute of Physical Chemistry IG Murgulescu, Romanian Academy, Spl. Independentei 202, Bucharest, Romania*
[d] *IPCF/CNR, via G. Moruzzi 1, Pisa, I56124, Italy, IPCF/CNR, via G. Moruzzi 1, Pisa, I56124, Italy. E-mail: fortunelli@ipcf.cnr.it*

reports the comparison of the results about supported clusters obtained by the different parametrizations of the Ni–Ni interactions. Section 5 compares the structures of free and supported Ni nanoparticles and section 6 contains the conclusions.

2. Model and parameter fitting

Following ref. 24, in the atomistic model for Ni/MgO(001) the potential energy E_i of the ith Ni atom is given by the sum of two contributions

$$E_i = E_i^{sub} + E_i^{coh}. \quad (1)$$

The total energy of the cluster is $E = \sum E_i \cdot E_i^{sub}$ is due to the substrate, which is kept rigid. E_i^{sub} depends on the coordinates $\mathbf{r}_i$ of the atom and on the number Z_i of its nearest Ni neighbours. The functional form of E_i^{sub}, together with a description of the fitting procedure, can be found in refs. 19 and 24. The fitting procedure is based on density-functional theory calculations. The parameter values for E_i^{sub} can be found in ref. 25.

E_i^{coh} is due to the nickel–nickel part of the interaction. It is a many-body term which depends on the ensemble $\{\mathbf{r}\}$ of the coordinates of all Ni atoms. Its functional form is derived within the second-moment approximation to the tight-binding model[26,27] and reads:

$$E_i^{coh} = E_i^{b} + E_i^{r} \quad (2)$$

with

$$E_i^{r} = \sum_{j \neq i, r_{ij} < r_c} A \exp\left[-p\left(\frac{r_{ij}}{r_0} - 1\right)\right]; \quad (3)$$

$$E_i^{b} = -\left\{\sum_{j \neq i, r_{ij} < r_c} \xi^2 \exp\left[-2q\left(\frac{r_{ij}}{r_0} - 1\right)\right]\right\}^{\frac{1}{2}}; \quad (4)$$

where r_{ij} is the distance between atoms i and j and $r_0 = 2.49$ Å is the nearest-neighbour distance in bulk Ni. r_c is the cut-off radius, which, as we shall see in the following, is different depending on the parametrization of the potential. The parameter set (A, ξ, p, q) is usually fitted to experimental bulk quantities.

Here we fit two different parameter sets, SET1 and SET2 (see Table 1), and compare them to the parameter sets fitted by Cleri and Rosato (CR)[28] and López and Jellinek (LJ).[29] As a further reference, we compare the outcomes of our semi-empirical tight-binding parametrizations to the embedded atom potentials for Ni parametrized by Voter-Chen[30] and Mishin-Farkas[31] (EA-VC and EA-MF, respectively).

Typical target experimental properties for the parametrization of atomistic metal potentials are the binding energy E_{bind}, the bulk modulus B and a set of independent elastic constants. This is the approach followed by CR and LJ. The EA-VC set of target properties includes also the vacancy formation energy, and the EA-MF potential complements this experimental set of target properties with the vacancy migration energy, the intrinsic stacking fault energy and the phonon-dispersion relations.

The choice of the targets for the potential parametrization is crucial in determining the reliability of the potential and it may depend on its specific applications. SET1 and SET2 potentials aim at predicting the stable structures of Ni clusters on MgO(001) for varying cluster size. The presence of the highly-mismatched oxide substrate is expected to influence the Ni–Ni nearest-neighbour distance, especially close to the oxide interface, and possibly the crystal structure of the supported particle. It is thus important that the metal-metal interaction accurately reproduces (i) the experimental Ni nearest-neighbour distance and (ii) the experimental value of the energy difference (per atom) $\Delta E_{hcp-fcc}$ between hcp and fcc bulk lattice. Based on these observations, in SET1 we fit the equilibrium nearest neighbour distance in bulk Ni, the bulk binding energy per atom E_{bind}, the bulk modulus B and the experimental value of the energy difference (per atom) $\Delta E_{hcp-fcc}$ between hcp and fcc bulk phases. SET1 was employed in ref. 17, giving results in very good agreement with the experimental data. In SET2, the only difference is that the reference value for $\Delta E_{hcp-fcc}$ is taken from DF calculations (see ref. 17 for details on the DF methodology).

The energy difference between hcp and fcc is known[28] to depend upon the choice of the cut-off radius of the potential. Following ref. 28, we choose r_c equal to the 5th-neighbour distance in bulk Ni. Then the potential is smoothly decreased to zero between the 5th and 6th neighbour distances by a polynomial function. This choice of the cutoff distance insures the right sign of the energy difference between fcc and hcp bulk phases. On the other hand, in LJ parametrization, r_c corresponds to the 12th-neighbour distance.

SET1 and SET2 potentials can be tested against properties which have not been used as targets for the parametrization, but are expected to play an important role in shaping the structure of oxide-adsorbed clusters. Two reference quantities have been selected, namely surface energies and interatomic distances of low-coordinated atoms. The former, together with the interface energy, determine the cluster shape according to the Wulff–Kaishew construction.[1] The latter can be more important in shaping small-size clusters, where the surface to volume ratio, and thus the number of low-coordinated atoms, are large.

The results in Table 2 show that all potentials correctly reproduce the experimental values of the nearest-neighbor distance r_0, of the binding energy per atom E_{bind} and of the bulk modulus B. $\Delta E_{hcp-fcc}$ has the correct sign for all potentials with the exception of LJ parametrization, for which fcc and hcp bulk phases are almost degenerate with a slight preference for hcp. CR parametrization gives $\Delta E_{hcp-fcc}$ with the correct sign, but it is five and three times larger than the experimental and DF results, respectively. Surface energies are of the correct magnitude range (compared to the average experimental result) and reasonably reproduce the anisotropy of DF calculations. However, CR parametrization somewhat overestimates surface energies whereas EA-VC and EA-MF potentials underestimate them. We note also that CR parametrization gives a weaker anisotropy of surface energies, with (001) and (111) faces nearly degenerate. The best results for nearest-neigbour distances in small clusters are obtained by SET1 followed by SET2.

Table 1 Parameter sets for Ni–Ni interaction. A and ξ are in eV. CR and LJ sets are taken from refs. 28 and 29 respectively

Parameter set	p	q	A	ξ
SET1	11.7300	1.93000	0.084470	1.404973
SET2	12.5800	1.75000	0.071531	1.327773
CR	16.9990	1.18900	0.037600	1.070000
LJ	12.6788	1.88351	0.076766	1.364235

We note that, according to the Wulff–Kaishew construction,[1,19,20] both the correct magnitude and the correct anisotropy of surface energies are necessary to reproduce the correct cluster shapes in supported nanoparticles belonging to the crystalline motifs. Moreover, the correct reproduction of the bulk modulus and binding energy is crucial for obtaining a potential with a good *stickiness*.[43–45] The latter is the key parameter in the competition between the strained non-crystalline motifs and the crystalline structures. We show in the following that also $\Delta E_{\mathrm{hcp-fcc}}$ plays a crucial role in determining the shape of Ni nanodots on MgO(001).

3. Computational methodology

The global optimization searches are performed by the basin-hopping algorithm,[46] the parallel excitable walkers (PEW) algorithm, and the HISTO algorithm.[47,48] PEW and HISTO searches need the definition of a suitable order parameter. In the case of supported clusters we mostly use as order parameters the fraction of atoms that is in contact with the substrate. For free clusters, we preferentially employ the (5,5,5) signature of the common neighbour analysis, which has been shown to discriminate well between crystalline and non-crystalline nanoparticles in the size range of interest.[49] For any nanoparticle size N below 100 atoms, 3–5 unseeded searches of 50 000 steps each are performed. Unseeded searches are started from random positions in a cubic box (which is placed above the oxide surface for supported clusters). In the range $100 < N < 200$, we considered only sizes 100, 110, 120, ..., 200. For each size, at least 10 unbiased searches were performed. We ran 15 unbiased searches for sizes $N = 300$ and 500. Moreover, several shorter seeded searches are performed. Seeded searches may either start from structures pertaining to motifs found at nearby sizes (typically $N - 1$ and $N + 1$ atoms), or from structures found at the same size within searches by means of a different potential parametrization.[50]

For larger nanoparticle sizes, global optimization is still too cumbersome from the computational point of view. Therefore we resort to the comparison of selected structural motifs, which are built up with the aid of the Wulff–Kaishew construction.[1,19,20] This construction determines the optimal aspect ratio for a supported nanoparticle of a given size from the knowledge of the metallic surface energies and of the metal-substrate interface energy.

4. Supported nanoparticle structures

4.1 Structures for sizes $50 \leq N \leq 500$ atoms

Let us consider first the results obtained by means of SET1 parametrization. Our global optimization searches find that, in the size range between 50 and 100 atoms, five structural motifs are in competition (see Fig. 1): hcp structures, faulted hcp (hcpfcc) structures, strongly distorted fcc structures in cube-on-cube epitaxy with the substrate (fcc001), icosahedral (I_{h}) and decahedral (D_{h}) fragments. The hcp nanodots present vertical close-packed planes which run parallel to the magnesium-oxide row (along the [100] or [010] directions) in the substrate and adhere to the substrate with a typical zig-zag pattern.[4,17]

The hcpfcc structures are made of vertical close-packed planes along the [100] or [010] direction of the substrate, in the same way as in hcp nanodots. However, the hcpfcc structures have faults in the ...ABAB... stacking of the

Table 2 Bulk binding energy per atom, E_{bind}, equilibrium bulk nearest-neighbour distance, r_0, bulk modulus, B, energy difference between hcp and fcc bulk phases (per atom), $\Delta E_{\mathrm{hcp-fcc}}$, surface energies, $\gamma_{(111)}$, $\gamma_{(001)}$, $\gamma_{(110)}$, equilibrium distances in the dimer, trimer and tetrahedral tetramer, r_2, r_3, r_4. DFT, SET1 and SET2 results are from this work, unless otherwise specified. CR results for E_{bind}, r_0, and B are taken from ref. 28, whereas other quantities were calculated in this work. LJ results for E_{bind}, r_0, and B are taken from ref. 29, whereas other quantities were calculated in this work. EAM-MF results are from ref. 31 and EAM-VC results are from ref. 30

	Exp.	DFT	SET1	SET2	CR	LJ	EA-MF	EA-VC
E_{bind}/eV	−4.44[a]/−4.45[b]	−4.79	−4.44	−4.44	−4.435	−4.44	−4.45	−4.45
r_0/Å	2.49[a]	2.485	2.49	2.49	2.49	2.489	2.489	2.489
B/GPa	181[a]	253	181	181	189	194	181	181
$\Delta E_{\mathrm{hcp-fcc}}$/eV	0.01[d]	0.015	0.0101	0.0151	0.05	−0.00047	0.02	0.01
$\gamma_{(111)}$/mJ m^{-2}		1758	1912	2060	2687	2003	1629	1621
$\gamma_{(001)}$/mJ m^{-2}	$\langle\gamma\rangle$ = 2280[e]	2043	2009	2143	2672	2106	1878	1754
$\gamma_{(110)}$/mJ m^{-2}		2094	2163	2299	2819	2255	2049	1977
r_2/Å	2.154[f]	2.23–2.29[g] 2.08–2.19[h] 2.13[i]	2.23	2.27	2.38	2.36	2.45	
r_3/Å		2.15–2.28[h] 2.26[i]	2.32	2.35	2.43	2.34	2.44	
r_4/Å		2.15–2.36[h] 2.29[j]	2.37	2.39	2.47	2.39	2.45	

Experimental data are taken from the following sources:[a] from ref. 32; [b] From ref. 33; [c] From ref. 34; [d] From ref. 35; [e] The experimental result $\langle\gamma\rangle$ is the average value on different orientations taken from refs. 36 and 37; [f] From ref. 38; DFT data are taken from the following sources: [g] From ref. 39; [h] From ref. 40; [i] From ref. 41; [j] From ref. 42.

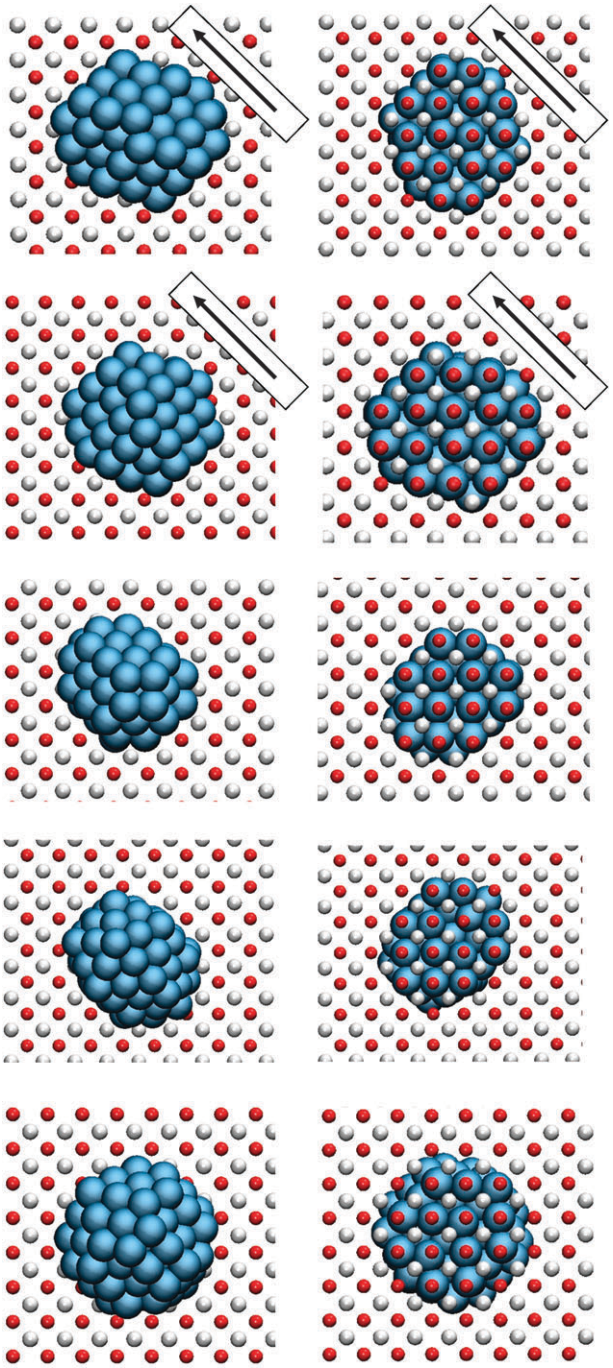

Fig. 1 Top (left column) and bottom view (right column) of nanoparticles belonging to the five structural motifs. First row: hcp motif, size 90. The close-packed planes are perpendicular to the MgO surface and run perpendicular to the arrow in the figures. There are six of such planes, in an ABABAB stacking sequence. Second row: hcpfcc motif, size 90. Close-packed planes present the same orientation as in the hcp motif. The planes run perpendicular to the arrow. There are six planes in an ABABCB stacking sequence. Third row: fcc001 motif, size 52. Fourth row: I_h motif, size 63. Fifth row: D_h motif, size 90.

close-packed planes. Around these faults, the atomic arrangement is fcc-like. In some cases (which are more likely to be found as size increases) the nanoparticles can present a larger proportion of fcc than of hcp regions.

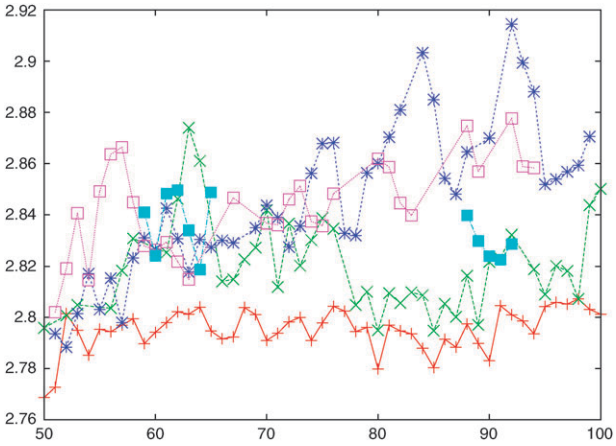

Fig. 2 Δ (eV) as a function of N for hcp (+), hcpfcc (×), fcc001 (*) I_h (□) and D_h (■) motifs. The lines are only guides to the eye.

In Fig. 2 we report the quantity Δ, defined as[51]

$$\Delta = \frac{E - NE_{\text{bind}}}{N^{2/3}} \tag{5}$$

which represents approximately the excess energy of the nanoparticle with respect to a piece of bulk Ni of the same size, divided by the number of surface/interface atoms. This quantity is useful to compare the stability of nanoparticles of different sizes, both in the gas phase and on surfaces.[19,44,51]

All global minima in the range $50 \leq N \leq 100$ belong to the hcp motif, with the single exception of size 52, for which a fcc001 structure prevails (see Fig. 1). However, fcc001 structures become quite unfavourable as size increases, whereas the hcpfcc motif, which is never the most favourable, is rather close in energy to the hcp motif for $N > 70$. I_h fragments are the second-lowest in energy only in the range 60–65 atoms, where a quite regular I_h fragment is found (see Fig. 1), and for a few more isolated sizes. Finally, our searches have been able to find D_h fragments only in limited size ranges, $59 \leq N \leq 65$ and $88 \leq N \leq 92$, where these structures are quite symmetric. The first and the second size range correspond to fragments of the gas-phase 75-atom and 101-atom Marks decahedra, respectively. In these ranges, D_h structures compete for the second-lowest motif, being however much higher in energy than hcp clusters. In the range $100 \leq N \leq 200$ we considered only sizes 110, 120. *etc*. In all cases, the lowest energy structures were hcp. With increasing size, the occurrence of faults in the hcp stacking becomes more and more favourable, so that hcpfcc clusters may become lower in energy than hcp ones. This is the case for $N = 500$.[17]

In the range $N \leq 500$, parametrizations SET2 and LJ do not give qualitatively different results from SET1. In SET2, the creation of faults in hcp nanodots is somewhat more favourable, whereas in LJ it is not favourable. In any case, the dominant motif is hcp, in competition with hcpfcc when the size increases in the case of SET2. The occurrence of faults in the hcp nanodots with increasing size has been observed in experiments.[4]

On the other hand, CR parametrization gives qualitatively different results. We have considered $N = 50$, 60, 70, 80, 90, 100, 110, 150, 200, 300. The occurrence of faults in the hcp

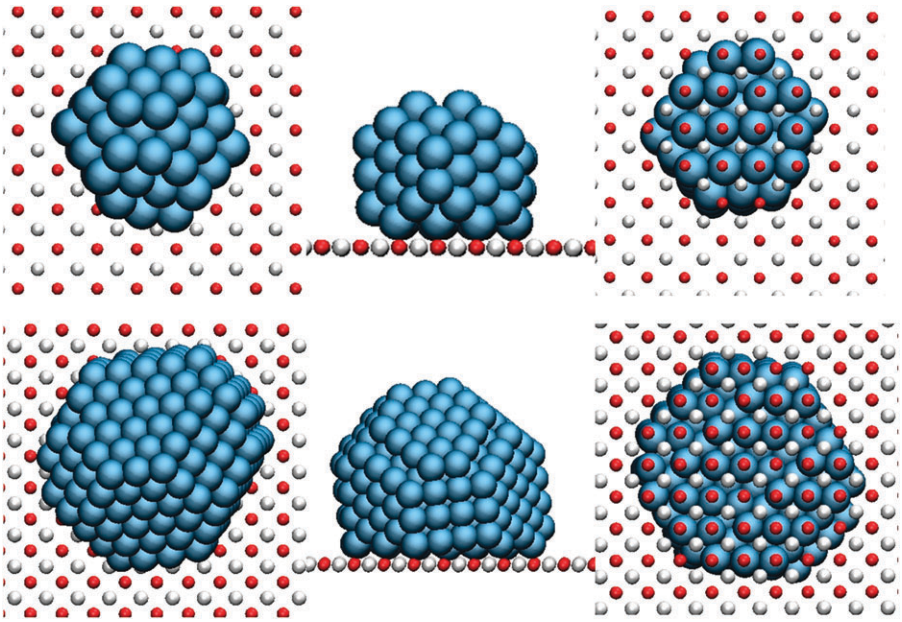

Fig. 3 Lowest-energy structures according to CR parametrization. Top row: hcpfcc cluster of 100 atoms. Bottom row: tilted fcc cluster of 364 atoms.

stacking is so favourable that we have never found pure hcp structures as the lowest in energy. For $N = 50$, a fcc001 structure prevails, whereas hcpfcc structures prevail for the remaining sizes. In these structures, the hcp zones tend to become smaller and smaller. For larger nanodots, a new motif appears, as shown in Fig. 3 for $N = 364$. This is a tilted fcc cluster, whose close-packed planes are not perpendicular to the substrate. The cluster is cut in such a way that its basal plane is still in good registry with the substrate. In summary, according to CR parametrization, hcp nanodots should not be observed. Faulted hcp nanodots are likely for very small sizes. This is not in agreement with the experimental observations.

4.2 Crossover from hcp to fcc structures

With increasing size, volume energy terms, deriving from the energetic cost of the hcp phase, lead to a destabilization of the latter to the advantage of the fcc001 phase. This has been experimentally observed.[4] In ref. 17 we compared the hcp and the fcc001 motif at increasing sizes within our model with SET1 parametrization. The clusters were built with the aid of the Wulff–Kaishew construction. However, fcc001 clusters were further optimized by short global optimization runs, which were intended to look for the appearance of dislocations. Dislocations were found, but they did not change the energetic ordering in an appreciable way. A crossover from hcp to fcc001 in the size range between 2000 and 2500 atoms was found, corresponding to a nanoparticle diameter of about 4.5 nm, in good agreement with the experimental estimate of a crossover for a diameter of 5 nm.[4]

Here we compare SET1, SET2, CR and LJ parametrizations for what concerns the hcp → fcc001 crossover size. The results are shown in Fig. 4.

SET2 parameters predict a crossover size of about 1000 atoms, corresponding to cluster diameters slightly larger than

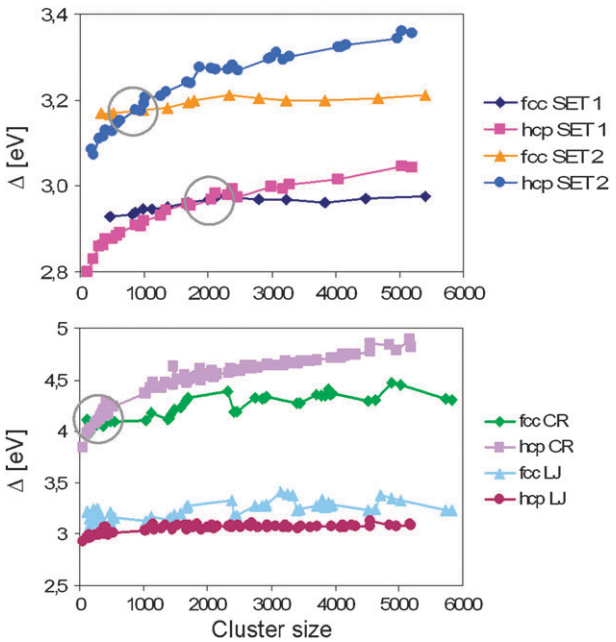

Fig. 4 Δ for hcp and fcc001 structures according to the four different potential parametrizations. The crossover from hcp to fcc001 structures occurs only for SET1, SET2 and CR (note however that in the CR case it is indeed a crossover from hcpfcc to fcc001 structures, since pure hcp clusters are never the most favourable). Crossover ranges are enclosed in circles.

3 nm. This crossover size derives essentially from the larger value of $\Delta E_{\mathrm{hcp-fcc}}$ (see Table 2), and it is significantly smaller than what is experimentally observed. However we cannot rule it out completely because kinetic effects are difficult to disentangle from energetic effects in the experiments. These kinetic effects may generate large hcp clusters as growth

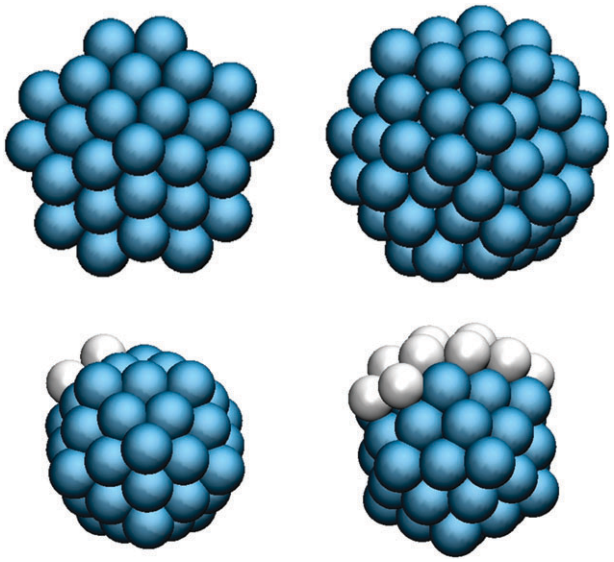

Fig. 5 Structures of gas-phase clusters. Top row: decahedral lowest-energy structures for sizes 75 (left) and 101 (right). The supported 90-atom decahedron of Fig. 1 is a fragment of the latter. Bottom row: two views of the lowest-energy structure at size 65. It is a 55-atom icosahedron capped by an island in anti-Mackay stacking. Atoms of the island are depicted in light gray.

structures, which are not the lowest in energy but keep the hcp motif because they grow from smaller stable hcp clusters.

CR parameters predict that hcp structures are lower in energy than fcc001 structures for $N < 300$, *i.e.* for clusters not larger than 2 nm. Moreover, in this size range, hcpfcc clusters are more favourable than pure hcp ones. This means that, according to CR parametrization, hcp structures should never be observed, in disagreement with the experimental data.

Finally, LJ parameters do not predict any crossover up to 6000 atoms at least. We expect indeed that the crossover should never take place, due to the slightly lower energy of the hcp bulk phase compared to the fcc phase. Also in this case, the prediction disagrees with the experiments.

These findings show the sensitivity of the resulting cluster shapes to the value of $\Delta E_{\mathrm{hcp-fcc}}$, which must be of the right sign and order of magnitude to have an at least qualitative agreement with the experimental observations.

5. Comparison of free and supported nanoparticle morphologies

Here we consider the morphologies of gas-phase clusters according to SET1 parametrization. We consider the size range from 38 up to about 100 atoms. The dominant motif in this size range is icosahedral. In Fig. 5 we report the lowest-energy structure found for $N = 65$. This consists of the *magic* icosahedron of 55 atoms capped by an island with anti-Mackay stacking. With increasing size, the best islands shift to the usual Mackay stacking. Exceptions to the predominance of icosahedra are size 38, at which an fcc truncated octahedron is found, and sizes around 75 and 101, where we find Marks decahedra (see Fig. 5).

When comparing gas-phase and supported nanoparticles, it turns out that the structures of the latter are crucially determined by the interaction with the substrate. Fragments of gas-phase clusters were found in the optimization on the MgO support. For example, around size 90, the supported decahedral structure is a fragment of the gas-phase decahedral cluster. However these gas-phase fragments are always much higher in energy than the best supported hcp structures.

6. Conclusions

In summary, we have shown that the prediction of the structures of oxide-supported nanoparticles is quite sensitive to the details of the atomistic model which is employed in the description. From the Wulff–Kaishew construction we know that atomistic models must give the correct values of free surface energies of nickel and of the interfacial adhesion energy with the substrate. In our model, free surface energies of nickel compare well to density-functional data and to the averaged experimental value. The interface energy is directly fitted to DF data. However, for Ni/MgO(001) this is not sufficient: also the correct $\Delta E_{\mathrm{hcp-fcc}}$ must be reproduced by the model, because this quantity is crucial in determining the occurrence of the crossover from hcp to fcc001 structures and the crossover size. For this reason, a qualitative agreement is obtained by employing SET1 or SET2 parametrizations. These differ only in fitting either the experimental or the density-functional values of $\Delta E_{\mathrm{hcp-fcc}}$. If we assume that experimental structures are indeed lowest-energy structures (*i.e.* if we assume that thermodynamic and kinetic effects are negligible), SET1 should be preferred, since it is in good quantitative agreement with the experimental data.

Finally, we note that the interaction between Ni and MgO is crucial in determining cluster structures. The effect of the substrate is even more important than in Pd or Pt/MgO, because it induces not only a reshaping of the structures compared to those in the gas phase, but also a change in the lattice type. This is due both to the strong adhesion of Ni to the substrate (which is present also in Pd and Pt/MgO) and to the huge lattice mismatch, which is a peculiar feature of Ni/MgO.

Important points that deserve further analysis for this system are those related to the effects of temperature on nanoparticle structures. Since the nanodots were experimentally grown on MgO at 120 °C,[4] the hcp structures are preserved up to this temperature at least, which is however likely to be well below the melting temperature of the nanodots. Whether further heating could lead to structural solid–solid transformations below melting is still an open issue.

Acknowledgements

R. F. acknowledges support from Italian MIUR for the PRIN Project No. 2007LN873M_003. The authors acknowledge support from CINECA and CNR-INFM for the project "Properties of Exotic Phases of Metal-on-Oxide Nanodots".

References

1 C. R. Henry, *Prog. Surf. Sci.*, 2005, **80**, 92.
2 J. Libuda and H.-J. Freund, *Surf. Sci. Rep.*, 2005, **57**, 157.
3 B. Pauwels, G. V. Tendeloo, W. Bouwen, L. T. Kuhn, P. Lievens, H. Lei and M. Hou, *Phys. Rev. B: Condens. Matter Mater. Phys.*, 2000, **62**, 10383.
4 W. Tian, H. P. Sun, X. Q. Pan, J. H. Yu, M. Yeadon, C. B. Boothroyd, Y. P. Feng, R. A. Lukaszew and R. Clarke, *Appl. Phys. Lett.*, 2005, **86**, 131915.
5 P. Nolte, A. Stierle, N. Kasper, N. Y. Jin-Phillipp, H. Reichert, A. Rühm, J. Okasinski, H. Dosch and S. Schöder, *Phys. Rev. B: Condens. Matter Mater. Phys.*, 2008, **77**, 115444.
6 O. Robach, G. Renaud and A. Barbier, *Phys. Rev. B: Condens. Matter Mater. Phys.*, 1999, **60**, 5858.
7 C. Revenant, G. Renaud, R. Lazzari and J. Jupille, *Nucl. Instrum. Methods Phys. Res., Sect. B*, 2006, **246**, 112.
8 S. Sao-Joao, S. Giorgio, C. Mottet, J. Goniakowski and C. R. Henry, *Surf. Sci.*, 2006, **600**, L86.
9 J. Olander, R. Lazzari, J. Jupille, B. Mangili, J. Goniakowski and G. Renaud, *Phys. Rev. B: Condens. Matter Mater. Phys.*, 2007, **76**, 075409.
10 J. Oviedo, J. F. Sanz, N. López and F. Illas, *J. Phys. Chem. B*, 2000, **104**, 4342.
11 M. Moseler, H. Häkkinen and U. Landman, *Phys. Rev. Lett.*, 2002, **89**, 176103.
12 C. Mottet, J. Goniakowski, F. Baletto, R. Ferrando and G. Tréglia, *Phase Transitions*, 2004, **77**, 101.
13 G. Rossi, C. Mottet, F. Nita and R. Ferrando, *J. Phys. Chem. B*, 2006, **110**, 7436.
14 C. Mottet and J. Goniakowski, *J. Comput. Theor. Nanosci.*, 2007, **4**, 326.
15 G. Barcaro, A. Fortunelli, F. Nita and R. Ferrando, *Phys. Rev. Lett.*, 2005, **95**, 246103.
16 G. Barcaro, A. Fortunelli, G. Rossi, F. Nita and R. Ferrando, *Phys. Rev. Lett.*, 2007, **98**, 156101.
17 R. Ferrando, G. Rossi, F. Nita, G. Barcaro and A. Fortunelli, *ACS Nano*, 2008, **2**, 1849.
18 G. Barcaro and A. Fortunelli, *J. Chem. Theory Comput.*, 2005, **1**, 972.
19 R. Ferrando, G. Rossi, A. C. Levi, Z. Kuntová, F. Nita, G. Barcaro, A. Fortunelli, A. Jelea, C. Mottet and J. Goniakowski, *J. Chem. Phys.*, 2009, **130**, 174702.
20 J. Goniakowski, A. Jelea, C. Mottet, G. Barcaro, A. Fortunelli, Z. Kuntová, F. Nita, A. C. Levi, G. Rossi and R. Ferrando, *J. Chem. Phys.*, 2009, **130**, 174703.
21 R. Ferrando, G. Barcaro and A. Fortunelli, *Phys. Rev. Lett.*, 2009, **102**, 216102.
22 G. Barcaro, R. Ferrando, A. Fortunelli and G. Rossi, *J. Phys. Chem. Lett.*, 2010, **1**, 111.
23 S. M. Woodley and R. Catlow, *Nat. Mater.*, 2008, **7**, 937.
24 W. Vervisch, C. Mottet and J. Goniakowski, *Phys. Rev. B: Condens. Matter Mater. Phys.*, 2002, **65**, 245411.
25 C. Mottet and J. Goniakowski, http://www.cinam.univ-mrs.fr/gModel/webparam.pdf.
26 F. Cyrot-Lackmann and F. Ducastelle, *Phys. Rev. B: Solid State*, 1971, **4**, 2406.
27 R. P. Gupta, *Phys. Rev. B: Condens. Matter*, 1981, **23**, 6265.
28 F. Cleri and V. Rosato, *Phys. Rev. B: Condens. Matter*, 1993, **48**, 22.
29 M.-J. López and J. Jellinek, *J. Chem. Phys.*, 1999, **110**, 8899.
30 A. F Voter and S. P. Chen, in *High temperature ordered inter metallic alloys*, ed. R. W. Siegel, J. R. Weertman and R. Sundan, MRS Symposia Proceedings, Materials Research Society, Pittsburgh, 1987, vol. 82, p. 175.
31 Y. Mishin, D. Farkas, M. J. Mehl and D. A. Papaconstantopoulos, *Phys. Rev. B: Condens. Matter Mater. Phys.*, 1999, **59**, 3393.
32 C. Kittel, *Introduction to Solid State Physics*, University of California, Berkeley, 2005.
33 *Metal Reference Book*, ed. C. J. Smith, Butterworth, London, 1976.
34 G. Simons and H. Wang, *Single Crystal Elastic Constants and Calculated Aggregate Properties*, MIT Press, Cambridge, MA, 1977.
35 A. T. Dinsdale, *CALPHAD: Comput. Coupling Phase Diagrams Thermochem.*, 1991, **15**, 317.
36 L. E. Murr, *Interfacial Phenomena in Metals and Alloys*, Addison-Wesley, Reading, MA, 1975.
37 W. R. Tyson and W. R. Miller, *Surf. Sci.*, 1977, **62**, 267.
38 J. C. Pinegar, J. D. Langenberg, C. A. Arrington and E. M. Spain, *J. Chem. Phys.*, 1995, **102**, 666.
39 C. V. Diaconu, A. E. Cho, J. D. Doll and D. L. Freeman, *J. Chem. Phys.*, 2004, **121**, 10026.
40 G. López Arvizu and P. Calaminici, *J. Chem. Phys.*, 2007, **126**, 194102.
41 M. C. Michelini, R. P. Diez and A. H. Jubert, *Comput. Mat. Sci.*, 2004, **31**, 292.
42 L. Giordano, J. Goniakowski and G. Pacchioni, *Phys. Rev. B: Condens. Matter Mater. Phys.*, 2001, **64**, 075417.
43 J. P. K. Doye and D. J. Wales, *J. Chem. Phys.*, 1995, **102**, 9659.
44 F. Baletto, R. Ferrando, A. Fortunelli, F. Montalenti and C. Mottet, *J. Chem. Phys.*, 2002, **116**, 3856.
45 F. Baletto and R. Ferrando, *Rev. Mod. Phys.*, 2005, **77**, 371.
46 D. J. Wales and J. P. K. Doye, *J. Phys. Chem. A*, 1997, **101**, 5111.
47 G. Rossi and R. Ferrando, *Chem. Phys. Lett.*, 2006, **423**, 17.
48 G. Rossi and R. Ferrando, *J. Phys.: Condens. Matter*, 2009, **21**, 084208.
49 F. Baletto, C. Mottet and R. Ferrando, *Phys. Rev. B: Condens. Matter Mater. Phys.*, 2001, **63**, 155408.
50 R. Ferrando, A. Fortunelli and R. L. Johnston, *Phys. Chem. Chem. Phys.*, 2008, **10**, 640.
51 C. L. Cleveland and U. Landman, *J. Chem. Phys.*, 1991, **94**, 7376.

